

Rubisco condensate formation by CcmM in β -carboxysome biogenesis

H. Wang^{1,3}, X. Yan^{1,3}, H. Aigner^{1,4}, A. Bracher¹, N. D. Nguyen², W. Y. Hee², B. M. Long², G. D. Price², F. U. Hartl¹ and M. Hayer-Hartl^{1,*}

¹Max Planck Institute of Biochemistry, Department of Cellular Biochemistry, Martinsried, Germany.

²Australian Research Council Centre of Excellence for Translational Photosynthesis, Research School of Biology, The Australian National University, Acton, Australia.

³These authors contributed equally

⁴Present address: KWS SAAT SE, Einbeck, Germany.

*Correspondence to: M. Hayer-Hartl, e-mail: mhartl@biochem.mpg.de

Compartmentalization of enzymes is a cellular strategy to regulate metabolic pathways and increase their efficiency¹. The α - and β -carboxysomes of cyanobacteria contain Ribulose-1,5-bisphosphate carboxylase/oxygenase (Rubisco), a complex of 8 large (RbcL) and 8 small (RbcS) subunits, and carbonic anhydrase (CA)²⁻⁴. Since the proteinaceous carboxysome shell provides a barrier to the diffusion of CO₂ but not HCO₃⁻ (ref. 5), CA generates high concentrations of CO₂ for carbon fixation by Rubisco⁶. The shell also prevents access to reducing agents, generating an oxidizing environment⁷⁻⁹. Formation of β -carboxysomes involves aggregation of Rubisco by the protein CcmM¹⁰, which exists in two forms: Full-length CcmM (M58 in *Synechococcus elongatus* PCC7942) containing a CA-like domain⁸ followed by three Rubisco small subunit-like (SSUL) modules connected by flexible linkers, and M35, lacking the CA-like domain¹¹. It has long been speculated that the SSUL modules interact with Rubisco by replacing RbcS²⁻⁴. Here we reconstituted the Rubisco:CcmM complex and solved its structure. Contrary to expectation, the SSUL modules do not replace RbcS, but bind close to the equatorial region of Rubisco between RbcL dimers, linking Rubisco molecules and inducing phase separation into a liquid-like matrix. Disulfide bond formation in SSUL increases the network flexibility and is required for carboxysome function *in vivo*. Importantly, the formation of the liquid-like condensate of Rubisco is mediated by dynamic interactions with the SSUL domains, rather than by low complexity sequences, which typically mediate liquid-liquid phase separation in eukaryotes^{12,13}. Indeed, within the pyrenoid of eukaryotic algae, the functional homologue of carboxysomes, Rubisco has been shown to adopt a liquid-like state via interactions with the intrinsically disordered protein EPYC1¹⁴. Understanding carboxysome biogenesis will be important in efforts to engineer CO₂ concentrating mechanisms (CCM) in plants¹⁵⁻¹⁹.

To understand the function of CcmM in β -carboxysome biogenesis, we solved the crystal structure of the first SSUL domain (SSUL1) of CcmM from *Synechococcus elongatus* PCC7942 (*Se7942*) at 1.65 Å resolution (Fig. 1a, Extended Data Table 1a). Although the two chains of SSUL1 in the asymmetric unit of the crystal structure form a dimer, the protein is monomeric in solution (Extended Data Fig. 1a, b). While the backbone of SSUL1 resembles RbcS (PDB 1RSC) ($C\alpha$ r.m.s.d. 1.61–1.62 Å) (Fig. 1b), residues in RbcS, which make critical contacts with RbcL in the holoenzyme (PDB 1RBL), are not conserved in the SSUL modules (Extended Data Fig. 1c). A notable feature in SSUL1 is a short helical insertion ($\alpha 2$, residues 250–254) after β -strand βA , which replaces the A-B loop in RbcS (Fig. 1b). Besides helix $\alpha 2$, the exposed face of the β -sheet and the loop following helix $\alpha 2$ are highly conserved among SSUL sequences (Fig. 1c). The conserved SSUL surface contains two clusters of charged residues (Extended Data Fig. 1d). Another distinctive feature of SSUL1 is a disulfide bond between Cys261 and Cys279 (Fig. 1a). These cysteines are conserved in SSUL2 but not in SSUL3 (Extended Data Fig. 1c), suggesting that M35 (and M58) function might be redox-regulated. We also solved the crystal structure of the reduced SSUL1 (SSUL1_{red}) at 1.2 Å resolution (Fig. 1d, Extended Data Fig. 1e, Extended Data Table 1a). Except for the absence of the disulfide bond, the structures of SSUL1_{red} and oxidized SSUL1 (SSUL1_{ox}) are highly similar ($C\alpha$ r.m.s.d. 0.74–0.94 Å) (Extended Data Fig. 1f).

To investigate how Rubisco complexes are linked for β -carboxysome formation, we performed *in vitro* experiments with purified Rubisco (RbcL₈S₈) and M35 from *Se7942* (Extended Data Fig. 2a). Reduced and oxidized M35 (M35_{red} and M35_{ox}, respectively) were chosen to specifically analyze the role of the SSUL domains in this process. Surprisingly, when

the proteins were combined at a molar ratio of Rubisco:M35 at 1:8, the solution became turbid, suggesting aggregate formation. By monitoring turbidity we found that the Rubisco:M35_{red} complex formed with a $t_{1/2}$ of ~15 s at 25°C, and an apparent affinity (K_D^{app}) of M35 for Rubisco of ~0.2 μ M, while formation of the Rubisco:M35_{ox} complex was ~4-times slower ($t_{1/2}$ ~50 s) with K_D^{app} reduced to ~1.0 μ M (Fig. 1e, f). The Rubisco in complex with M35 is functionally active (Extended Data Fig. 2b). M35 neither interacted with RbcL₈ or RbcS alone (Fig. 1e), nor with chaperone-bound assembly intermediates²⁰⁻²² (Extended Data Fig. 2c).

We next generated variants consisting of one or two SSUL modules (Fig. 1g, Extended Data Fig. 2a) and performed turbidity assays under reducing conditions. No network formation was observed with the single SSUL constructs, M13-1, M13-2 or M13-3, either alone (Fig. 1h) or in combination (Extended Data Fig. 2d). M24-1/2 (SSUL1-SSUL2) mediated network formation, albeit with reduced efficiency ($t_{1/2}$ ~40 s) compared to M35_{red}, while M24-2/3 (SSUL2-SSUL3) failed to induce turbidity (Fig. 1h). To estimate the relative affinities of the SSUL modules for Rubisco, we analyzed their ability to displace M35_{red} from Rubisco:M35 complexes. Addition of excess M13-2 (25 μ M) resulted in loss of turbidity within seconds ($t_{1/2}$ ~7 s) (Fig. 1i), indicating that the M35-Rubisco interaction is highly dynamic. Dual-color fluorescence cross-correlation spectroscopy (dcFCCS) using M35 N-terminally labeled with the fluorophore NT-650-NHS (NT650-M35) and Rubisco labeled with Alexa Fluor™ 532 NHS ester (A532-Rubisco) confirmed that M35 was displaced from Rubisco by excess M13-2 (Extended Data Fig. 2e, f). M13-1 was only slightly less effective in dispersing the M35-Rubisco network, but dissociation was ~3-times slower (Fig. 1i). In contrast, excess M13-3 could not completely dissociate M35-Rubisco ($t_{1/2}$ ~20 s). Formation of the Rubisco network is therefore predominantly mediated by SSUL1 and SSUL2.

The interaction of M35_{red} with Rubisco was salt sensitive, consistent with the conserved SSUL surface being highly charged (Extended Data Fig. 1d). Binding was efficient at 50 mM KCl, as used above, but decreased at 100 mM KCl (Extended Data Fig. 3a). Interaction at physiological salt concentration was observed at 4-fold higher concentration of Rubisco and M35 (Extended Data Fig. 3b). The salt dependence of M35_{ox} was more pronounced, with addition of reducing agent restoring M35 function (Extended Data Fig. 3c, d). Rubisco interaction with M24-1/2 and M24-2/3 was also salt sensitive (Extended Data Fig. 3e, f). M24-2/3 interacted with Rubisco at very low salt, indicating that all SSUL modules can participate in network formation.

Liquid-liquid phase separation (LLPS) of proteins, mediated by low complexity amino acid sequences, underlies the formation of non-membrane bound compartments in eukaryotes^{12,13,23,24}. The dynamic nature of the Rubisco:M35 network suggested that these proteins undergo LLPS. To test this possibility, we analyzed the interaction of NT650-M35_{red} and A532-Rubisco by fluorescence microscopy. The proteins on their own (mixed 1:10 with unlabeled protein) were diffusely distributed (Fig. 2a). Combining Rubisco (0.25 μ M) and M35_{red} (1 μ M) induced demixing into round fluorescent condensates with an average Feret's diameter of \sim 1.3 μ m (Fig. 2a, Extended Data Fig. 4a). The fusion of these condensates is characteristic of liquid droplets²⁵ (Extended Data Fig. 4b). LLPS of Rubisco with M35_{ox} was considerably less efficient than with M35_{red}, with fewer and smaller droplets forming in a background of diffuse M35 (Extended Data Fig. 4c). Fluorescence recovery after photobleaching (FRAP) of the droplets showed a slower rate of recovery ($t_{1/2}$ \sim 130 s) with M35_{red} than with M35_{ox} ($t_{1/2}$ \sim 70 s) (Fig. 2b, c). Fluorescence recovery with M35_{ox} was incomplete (Fig. 2c), presumably limited by the rate of diffusion of unbleached M35_{ox} from the bulk into the smaller droplets. Addition of excess unlabeled single-SSUL construct, M13-2, dissolved the droplets

(Extended Data Fig. 4d). Thus, the multivalent M35 condenses Rubisco into a liquid matrix reminiscent of the behavior of Rubisco in the pyrenoid of green algae¹⁴. The Rubisco condensate is more dynamic under oxidizing conditions, the presumed state in the carboxysome⁷⁻⁹.

To investigate whether carboxysome function is redox-regulated, we expressed either wild-type (WT) CcmM or cysteine mutants (Fig. 3a) in the carboxysome-less $\Delta ccmM$ strain of *Se7942*, which requires high CO₂ for growth¹⁰. Expression of plasmid-encoded *ccmM* WT protein rescued this phenotype (Fig. 3b, Extended Data Fig. 5a). Disruption of the disulfide bond in either SSUL1 or SSUL2 (mutants C279S and C395S, respectively; Fig. 3a), resulted in a ~10- to 20-fold increase in CO₂ requirement and a ~2- to 2.5-fold longer doubling time (Fig. 3b, Extended Data Fig. 5a). A further increase in CO₂ requirement and a ~4-fold increase in doubling time was observed when the disulfide bonds were disrupted in both SSUL1 and SSUL2 (CcmM-4S) (Fig. 3b, Extended Data Fig. 5a). Rubisco amounts in cysteine mutant strains were comparable to WT, as observed upon fractionation into soluble and carboxysome-enriched (pellet) fractions (Fig. 3c, Extended Data Fig. 5b), indicating that the defect is due to CCM dysfunction. Analysis of the cysteine mutants by electron microscopy showed abnormal carboxysomes with an increased length to width ratio in some cells (Fig. 3d, Extended Data Fig. 5c). Furthermore, the number of carboxysomes per cell was significantly reduced in mutants C395S and CcmM-4S (Extended Data Fig. 5d). Together, these results suggest that disulfide-bond formation in the SSUL modules is critical for carboxysome biogenesis.

To define the structural basis of the M35_{red}-Rubisco interaction, we next performed cryo-electron microscopy (cryo-EM) and single particle analysis. Reference-free 2D class averages revealed additional density at the equator of Rubisco (Extended Data Fig. 6a, b). The extra-density appeared two-fold symmetric along the dyad axis between RbcL anti-parallel dimers in

the D4 symmetry-averaged map (Extended Data Fig. 6c). However, docking of two SSUL1 molecules into this density showed an overlap of their $\alpha 1$ helices, suggesting that binding of one module blocks the symmetry-related binding site. This is consistent with the SSUL density values in the D4 map being approximately half as high as those for the RbcL subunits (Extended Data Fig. 6c). Accordingly, density for only one SSUL module per symmetry-related binding site was observed in a focused 3D classification without symmetry (C1 map, Extended Data Fig. 6d, left scheme). To obtain a structural model of the Rubisco:SSUL complex, we extracted units comprising 2 RbcL, 2 RbcS and 2 SSUL for averaging (Extended Data Fig. 6d, main scheme). The resulting density map at 2.77 Å resolution shows one SSUL module bound asymmetrically in a cleft between RbcL dimers (Fig. 4a, Extended Data Fig. 6e, Extended Data Table 1b). The density of SSUL was well-defined (Extended Data Fig. 7a-d), resulting in a model with four SSUL modules bound per Rubisco (Fig. 4a, b).

Two interfaces with Rubisco can be distinguished: The more extensive interface I is formed by contacts of SSUL helix $\alpha 2$ and the loop that follows, which fill a pocket between RbcL dimers and the β CD loop of RbcS (Fig. 4c, Extended Data Fig. 7c). Specifically, three arginine residues (Arg251, Arg252, Arg254) and one phenylalanine (Phe253) of helix $\alpha 2$ contact the RbcL subunits lining the groove (RbcL-A, RbcL-B) and RbcS via salt-bridges and van-der-Waals contacts (Fig. 4c). Interface II involves mainly van-der-Waals interactions between the β C- β D hairpin of SSUL and the RbcL-B subunit (Fig. 4d, Extended Data Fig. 7d). The contact residues in SSUL are highly conserved between SSUL modules (Extended Data Fig. 1c). Mutation of the conserved Arg251 and Arg252 to Asp (interface I) in SSUL1, while preserving M35 structure, disrupted the function of M35 in Rubisco condensation (Extended Data Fig. 7e-

g). Network formation was critically dependent on the interaction of SSUL with RbcS (Extended Data Fig. 7f).

To visualize the distribution of Rubisco in the Rubisco:M35 matrix, we performed cryo-electron tomography (cryo-ET). We observed dense clusters of Rubisco complexes, with a median nearest neighbor distance of 150 Å (Extended Data Fig. 8a, b). Accordingly, the flexible ~30 residue linkers between SSUL modules (spanning up to ~110 Å), though not resolved, must adopt compact conformations. We also performed cryo-ET on Rubisco:M24-1/2 (at 2-fold lower protein concentration) and found a similar distribution of particle distances within clusters (Extended Data Fig. 8b, c), ruling out a random distribution.

Contrary to the previous model of β -carboxysome formation, the SSUL modules of CcmM do not displace the RbcS subunit but bind close to the equator of the Rubisco cylinder. The critical interaction of SSUL with the β CD loop of RbcS (Fig. 4e) explains the exquisite specificity of M35 for the holoenzyme. Disulfide bond formation in SSUL attenuates the affinity of M35 for Rubisco, a property that is critical for β -carboxysome function *in vivo*. The multivalency of M35 and the fluctuating nature of the individual interactions seem to be critical for liquid-like matrix formation, consistent with results obtained with modular model proteins^{26,27}. How the CA-like domain of M58 modulates phase separation and how shell formation is coordinated with Rubisco condensation are important questions for future research. Our analysis of the interactions required for condensation of Rubisco in β -carboxysomes may provide insight into the mechanism of α -carboxysome biogenesis²⁸.

References

1. Hinzpeter, F., Gerland, U. & Tostevin, F. Optimal compartmentalization strategies for metabolic microcompartments. *Biophys. J.* **112**, 767-779 (2017).

- 2 Espie, G. S. & Kimber, M. S. Carboxysomes: cyanobacterial Rubisco comes in small packages. *Photosynth. Res.* **109**, 7-20 (2011).
- 3 Rae, B. D., Long, B. M., Badger, M. R. & Price, G. D. Functions, compositions, and evolution of the two types of carboxysomes: polyhedral microcompartments that facilitate CO₂ fixation in cyanobacteria and some proteobacteria. *Microbiol. Mol. Biol. Rev.* **77**, 357-379 (2013).
- 4 Kerfeld, C. A. & Melnicki, M. R. Assembly, function and evolution of cyanobacterial carboxysomes. *Curr. Opin. Plant Biol.* **31**, 66-75 (2016).
- 5 Dou, Z. *et al.* CO₂ fixation kinetics of *Halothiobacillus neapolitanus* mutant carboxysomes lacking carbonic anhydrase suggest the shell acts as a diffusional barrier for CO₂. *J. Biol. Chem.* **283**, 10377-10384 (2008).
- 6 Price, G. D. & Badger, M. R. Expression of human carbonic anhydrase in the cyanobacterium *Synechococcus* PCC7942 creates a high CO₂-requiring phenotype : Evidence for a central role for carboxysomes in the CO₂ concentrating mechanism. *Plant Physiol.* **91**, 505-513 (1989).
- 7 Price, G. D., Coleman, J. R. & Badger, M. R. Association of carbonic anhydrase activity with carboxysomes isolated from the cyanobacterium *Synechococcus* PCC7942. *Plant Physiol.* **100**, 784-793 (1992).
- 8 Peña, K. L., Castel, S. E., de Araujo, C., Espie, G. S. & Kimber, M. S. Structural basis of the oxidative activation of the carboxysomal gamma-carbonic anhydrase, CcmM. *Proc. Natl. Acad. Sci. U.S.A.* **107**, 2455-2460 (2010).
- 9 Chen, A. H., Robinson-Mosher, A., Savage, D. F., Silver, P. A. & Polka, J. K. The bacterial carbon-fixing organelle is formed by shell envelopment of preassembled cargo. *PLoS One* **8**, e76127 (2013).
- 10 Long, B. M., Badger, M. R., Whitney, S. M. & Price, G. D. Analysis of carboxysomes from *Synechococcus* PCC7942 reveals multiple Rubisco complexes with carboxysomal proteins CcmM and CcaA. *J. Biol. Chem.* **282**, 29323-29335 (2007).
- 11 Ludwig, M., Sültemeyer, D. & Price, G. D. Isolation of *ccmKLMN* genes from the marine cyanobacterium, *Synechococcus* sp. PCC7002 (Cyanophyceae), and evidence that CcmM is essential for carboxysome assembly. *J. Phycol.* **36**, 1109-1119 (2000).
- 12 Hyman, A. A., Weber, C. A. & Julicher, F. Liquid-liquid phase separation in biology. *Annu. Rev. Cell Dev. Biol.* **30**, 39-58 (2014).
- 13 Banani, S. F., Lee, H. O., Hyman, A. A. & Rosen, M. K. Biomolecular condensates: organizers of cellular biochemistry. *Nat. Rev. Mol. Cell Biol.* **18**, 285-298 (2017).
- 14 Freeman Rosenzweig, E. S. *et al.* The eukaryotic CO₂-concentrating organelle is liquid-like and exhibits dynamic reorganization. *Cell* **171**, 148-162.e119 (2017).
- 15 Hanson, M. R., Lin, M. T., Carmo-Silva, A. E. & Parry, M. A. Towards engineering carboxysomes into C3 plants. *Plant J.* **87**, 38-50 (2016).
- 16 Ort, D. R. *et al.* Redesigning photosynthesis to sustainably meet global food and bioenergy demand. *Proc. Natl. Acad. Sci. U.S.A.* **112**, 8529-8536 (2015).
- 17 Price, G. D. *et al.* The cyanobacterial CCM as a source of genes for improving photosynthetic CO₂ fixation in crop species. *J. Exp. Bot.* **64**, 753-768 (2013).
- 18 Zarzycki, J., Axen, S. D., Kinney, J. N. & Kerfeld, C. A. Cyanobacterial-based approaches to improving photosynthesis in plants. *J. Exp. Bot.* **64**, 787-798 (2013).
- 19 Long, B. M. *et al.* Carboxysome encapsulation of the CO₂-fixing enzyme Rubisco in tobacco chloroplasts. *Nat. Commun.*, doi:10.1038/s41467-018-06044-0 (2018).
- 20 Bracher, A., Starling-Windhof, A., Hartl, F. U. & Hayer-Hartl, M. Crystal structure of a chaperone-bound assembly intermediate of form I Rubisco. *Nat. Struct. Mol. Biol.* **18**, 875-880 (2011).
- 21 Hauser, T. *et al.* Structure and mechanism of the Rubisco-assembly chaperone Raf1. *Nat. Struct. Mol. Biol.* **22**, 720-728 (2015).
- 22 Aigner, H. *et al.* Plant Rubisco assembly in *E. coli* with five chloroplast chaperones including BSD2. *Science* **358**, 1272-1278 (2017).

- 23 Cuevas-Velazquez, C. L. & Dinneny, J. R. Organization out of disorder: liquid-liquid phase separation in plants. *Curr. Opin. Plant Biol.* **45**, 68-74 (2018).
- 24 Wang, J. *et al.* A molecular grammar governing the driving forces for phase separation of prion-like RNA binding proteins. *Cell* **174**, 688-699.e616 (2018).
- 25 Alberti, S. *et al.* A user's guide for phase separation assays with purified proteins. *J. Mol. Biol.*, **430**, 4806-4820 (2018).
- 26 Li, P. *et al.* Phase transitions in the assembly of multivalent signalling proteins. *Nature* **483**, 336-340 (2012).
- 27 Banani, S. F. *et al.* Compositional control of phase-separated cellular bodies. *Cell* **166**, 651-663 (2016).
- 28 Cai, F. *et al.* Advances in understanding carboxysome assembly in *Prochlorococcus* and *Synechococcus* implicate CsoS2 as a critical component. *Life (Basel)* **5**, 1141-1171 (2015).

Acknowledgments

We thank S. Gärtner, R. Lange, N. Wischniewski and L. Rourke for technical assistance and D. Balchin and R. H. Wilson for critically reading the manuscript. We thank M. Strauss, J. Plitzko, F. Beck, S. Albert and Q. Guo (MPIB cryo-EM facility) for valuable input on data collection and processing, and the Centre for Advanced Microscopy (ANU) for assistance with electron transmission microscopy of cyanobacteria. We thank the staff at the MPIB Crystallization and Imaging facilities, and at the European Synchrotron Radiation Facility (ESRF) in Grenoble, France. This work was supported by a grant from the Deutsche Forschungsgemeinschaft (DFG) (SFB1035) to M.H.-H. and F.U.H., funding to G.D.P. from the Australian Government through the Australian Research Council Centre of Excellence for Translational Photosynthesis (CE1401000015), and the Minerva foundation of the Max Planck Society (M.H.-H.).

Author contributions

H.W. and X.Y. together with M.H.-H. and F.U.H. designed the experiments presented. H.W. performed most of the structural analyses by cryo-EM and tomography, including sample screening, grid preparation, data acquisition and single particle/tomography reconstructions, while X.Y. performed most of the biochemical experiments. H.A. cloned M35 and some of the

SSUL modules, performed initial biochemical experiments, and crystallized SSUL1. A.B. solved the crystal structures of SSUL1_{ox} and SSUL1_{red} and supervised the structural analysis by H.W. G.D.P, B.M.L, W.Y.H. and N.D.N. designed the cyanobacterial experiments and generated the pHUE-SSUL1 plasmid, with data collection conducted by N.D.N., W.Y.H. and B.M.L. M.H-H. conceived the project, participated in data interpretation and wrote the manuscript with contributions from F.U.H. and other authors.

Competing interests The authors declare no competing interests.

Additional information

Extended data is available for this paper at <https://>

Supplementary information is available for this paper at <https://>

Reprints and permission information is available at www.nature.com/reprints.

Correspondence and requests for materials should be addressed to M.H-H.

Figure legends

Fig. 1 | Crystal structure of SSUL1 and formation of Rubisco network by M35. **a**, Ribbon representation of thiol-oxidized SSUL1 from CcmM of *Se7942*. Two views rotated by 90° are shown. **b**, Alignment of SSUL1 (magenta) with RbcS (green) from *Se6301* (PDB 1RBL). Note that *Se7942* and *Se6301* have identical sequences for Rubisco and CcmM proteins. **c**, Surface conservation in the SSUL1, based on alignment of eight sequences. Orientation as in (a). Conserved residues in the interface with Rubisco (see Extended Data Fig. 1c) are indicated. **d**, Ribbon representation of thiol-reduced SSUL1. **e**, Kinetics of Rubisco network formation by turbidity assay ($A_{340\text{nm}}$) in buffer A at 25°C. Rubisco (0.25 μM), RbcL₈ (0.25 μM) or RbcS (2 μM) in the presence of M35_{red} or M35_{ox} (2 μM). Rubisco and M35 alone served as controls. A representative experiment is shown ($n=3$ independent experiments). **f**, Apparent binding affinity (K_D^{app}) of M35_{red} and M35_{ox} to Rubisco. Network formation of Rubisco was measured as in (e) at increasing concentrations of M35. Turbidity values reached after 10 min are plotted. Data are the mean \pm s.d. ($n=3$ independent experiments). **g**, Schematics of full-length M58 (CcmM) and M35, as well as M35 truncation constructs. **h**, Kinetics of Rubisco network formation analyzed as in (e). Rubisco (0.25 μM) was combined with M35 (2 μM) or the M35 variants M13-1 (6 μM), M13-2 (6 μM), M13-3 (6 μM), M24-1/2 (2 μM), and M24-2/3 (2 μM). A representative experiment is shown ($n=3$ independent experiments). **i**, Dissociation of the Rubisco:M35 network. Rubisco (0.25 μM) was combined with M35_{red} (1 μM) and network formation monitored by turbidity assay for 5 min, followed by addition of M13-1, M13-2 or M13-3 (25 μM each). The apparent $t_{1/2}$ of dissociation is indicated. Data are the mean \pm s.d. ($n=3$ independent experiments).

Fig. 2 | Condensation of Rubisco into a network with liquid-like properties. **a**, LLPS of Rubisco:M35. NT650-M35 and A532-Rubisco were mixed 1:10 with the respective unlabeled proteins at total concentrations of M35 and Rubisco of 1 μ M and 0.25 μ M, respectively. The proteins were imaged by fluorescence at 25°C either alone (panels 1 and 2) or in combination (panels 3-5). Droplets contained both M35 and Rubisco, as visualized by merging the fluorescence of NT650-M35 and A532-Rubisco (panel 5). Scale bar 10 μ m. A representative experiment is shown ($n=3$ independent experiments). **b-c**, Fluorescence recovery after photobleaching (FRAP) of Rubisco condensates formed by unlabeled Rubisco (0.5 μ M) and M35_{red} (**b**) or M35_{ox} (**c**) (2 μ M respectively, containing 10 % of the respective labeled NT650-M35). One representative condensate is shown before and after bleaching. The site of bleaching is marked by a dashed circle. Scale bar 2 μ m. The change in the fluorescence was analyzed as a function of time and the $t_{1/2}$ of fluorescence recovery is indicated as the mean \pm s.d ($n=15$ and $n=7$ for M35_{red} and M35_{ox}, respectively).

Fig. 3 | Role of disulfide bonds in SSUL in carboxysome function. **a**, Schematic representation of full-length M58 (CcmM) and M35 proteins with the positions of the disulfide bond forming cysteines in SSUL1 and SSUL2 domains indicated. **b**, Photosynthetic half-saturation constants as $K_{0.5}$ (mM C_i) and doubling times (h) for *Se7942* WT and cysteine mutants grown in air. $\Delta ccmM$ cells were analyzed alone or complemented with WT *ccmM* ($\Delta ccmM+ccmM$) or cysteine mutants. *, $p=0.01-0.05$; ***, $p<0.001$ (Tukey's multiple comparisons test). p -Values indicated for WT versus cysteine mutants ($K_{0.5}$: WT versus CcmM-4S $p<0.0001$, WT versus C279S $p=0.0218$; doubling time: WT versus CcmM-4S $p<0.0001$, WT versus C279S $p=0.0003$). Data are mean \pm s.e.m. of 3 biological repeats. **c**, Rubisco amounts in

carboxysome-enriched cell pellets and their corresponding supernatants in *Se7942* WT and cysteine mutants. Data are mean \pm s.e.m. of 3 biological repeats. **d**, Transmission electron micrographs of ultrathin sections of *Se7942* cells with WT *ccmM*, $\Delta ccmM$ (carboxysomeless), $\Delta ccmM$ complemented with either the WT *ccmM* ($\Delta ccmM+ccmM$), or with mutant C279S, C395S or CcmM-4S. Carboxysomes are indicated by arrowheads. Scale bar 200 nm. Representative micrographs are shown. Images are representative of carboxysomes from WT and mutant cell lines (WT $n=106$, $\Delta ccmM+ccmM$ $n=78$, C279S $n=106$, C395S $n=98$, CcmM-4s $n=104$; see Extended Data Fig. 5c).

Fig. 4 | Cryo-EM structure of Rubisco:M35 complexes. **a**, Density map of 3D-reconstruction from cryo-EM and single particle analysis of 2RbcL:2RbcS:SSUL units at 2.77 Å resolution (left) (Extended Data Fig. 6d, e) and the refined structural model in ribbon representation (right). The RbcL subunits in contact with SSUL are from adjacent anti-parallel RbcL dimers and are colored gold and pale yellow, RbcS in pale blue and SSUL in magenta. **b**, Model of the Rubisco:SSUL complex showing a hypothetical alternating arrangement of four SSUL modules (magenta). Side- and top-views are shown. One 2RbcL:2RbcS:SSUL unit is colored as in (a). **c-d**, Structural features of interface I (**c**) and II (**d**). Contact residues are indicated (see Extended Data Fig. 7c, d for details). **e**, Model of the liquid-like Rubisco:M35 matrix at different scales, from droplets to clusters to molecular contacts.

METHODS

No statistical methods were used to predetermine sample size. The experiments were not randomized, and the investigators were not blinded to allocation during experiments and outcome assessment.

Cloning, plasmids and strains. For generation of pHUE-SSUL1 the 267bp *ccmM*-SSUL1 region was synthesised to include an EcoRI site immediately upstream of base 673 of *ccmM* from *Se7942* (UniProtKB_Q03513) (context gaattccCTCAGTTCC) and a stop codon (taa) plus HindIII site immediately downstream of base 939 of *ccmM* (context GGTTCGGTTaaaagctt) cloned into EcoRI/HindIII sites of pHUE²⁹. After cleavage of the His₆-tagged product with deubiquitylating enzyme, this yielded a SSUL1 protein of 89 amino acids (amino acids 225-313 of M58) with three cryptic residues (Ser/Glu/Phe) at the N-terminus.

The *ccmM* gene (UniProtKB_A0A0H3JZU5) was amplified from genomic DNA of *Se6301* (*Se6301* is indistinguishable from *Se7942* in the *ccm* operon). Cyanobacteria from a 100 mL culture (OD₆₀₀ ~2) were washed once with fresh medium (BG-11) and then pelleted. Cells were suspended in 20 mM Tris-HCl pH 6.8. 1.2 mL of cell suspension and 300 mg of glass beads (0.5 mm diameter) were placed in a 2 mL tube and crushed in a bead beating homogenizer. After a clarifying spin the supernatant was mixed with an equal volume of extraction buffer (20 mM Tris-HCl pH 6.8, 1 M NaCl, 2 % SDS). The solution was centrifuged (21,000 rpm, 5 min at room temperature (RT)) and the supernatant combined with an equal volume of isopropanol, gently mixed by inversion, and placed on ice for 20 min. After centrifugation (21,000 rpm, 5 min, at RT), the pellet was washed with 500 µL 70 % (v/v) ethanol and dried (10 min at RT). The dried pellet was dissolved in 50 µL deionized water, centrifuged (21,000 rpm, 2 min at RT) and

stored at -20°C . From the DNA thus obtained, the full-length *ccmM* sequence was amplified by PCR and cloned into the pHUE vector²⁹. The shorter constructs were prepared by PCR from this plasmid and cloned into the vector pHUE. Plasmids, proteins and strains used or generated in this study are listed in Extended Data Table 2.

***SeRbcL₈S₈* preparation.** *SeRbcL₈* and *SeRbcS* were expressed and purified as previously described^{30,31}. The purified RbcL₈ core complexes and RbcS were mixed at a ratio of 1:16 and incubated at 25°C for 30 min. The RbcL₈S₈ complex was further purified by size-exclusion chromatography (Superdex200, GE Healthcare). Formation of assembled complexes was analyzed by 4–12 % Tris-Glycine gradient gels (Thermo Fisher).

Expression and purification of M35 and variants. M35 and truncation constructs were transformed into *E. coli* BL21 cells. Pre-cultures (5 mL) were grown in LB medium overnight at 37°C and 180 rpm. The pre-culture was added to one liter LB medium containing ampicillin ($100\text{ }\mu\text{g mL}^{-1}$), resulting in a final OD₆₀₀ of 0.05. When the cells reached an OD₆₀₀ of ~ 0.5 (37°C and 180 rpm), the culture was shifted to 18°C and IPTG (0.25 mM final concentration) and proteins expressed for ~ 16 h.

The cell pellet from 3 x 1 L cultures was resuspended in 50 mL buffer (50 mM Tris-HCl pH 8.0, 300 mM NaCl, 2 mM DTT, protease inhibitor, benzonase), and lysis performed using a Emulsiflex homogenizer (Avestin). The cell lysate was cleared by centrifugation (45 min, 40,000 rpm) and the supernatant loaded on a 5 mL Ni-NTA column equilibrated with buffer (50 mM Tris-HCl pH 8.0, 300 mM NaCl, 2 mM DTT). The His₆-ubiquitin fusion protein was eluted with buffer containing 250 mM imidazole. The ubiquitin moiety was cleaved overnight at 4°C using

the deubiquitylating enzyme Usp2 (Baker et al., 2005), in the presence of 5 mM DTT. After overnight digestion, the buffer was exchanged to 50 mM Tris-HCl pH 8.0, 50 mM NaCl and 2 mM DTT and loaded on a 5 mL Ni-NTA column. The eluted protein was further purified by size-exclusion chromatography (Sephacryl S-100) in buffer A (50 mM Tris-HCl pH 8.0, 50 mM KCl, 10 mM Mg(OAc)₂, 5 mM DTT) containing 10 % (v/v) glycerol. Fractions containing pure protein were concentrated, and aliquots were flash-frozen in liquid nitrogen for storage at –80°C.

Oxidized M35 and variants were purified as above in the absence of DTT. Disulfide bond formation occurred through air oxidation. The concentration of free thiol groups in the oxidized M35 was quantified by Ellman's Assay with the chemical 5,5'-dithio-*bis*-(2-nitrobenzoic acid)³². The purified proteins were >95 % pure as judged by SDS-PAGE (Extended Data Fig. 2a).

Turbidity assay. Measurements were performed at 25°C in buffer (50 mM Tris-HCl pH 8.0, 10 mM Mg(OAc)₂) containing different concentrations of KCl and in the absence or presence of 5 mM DTT as indicated in the figure legends. 100 µL reactions containing Rubisco (0.25 µM) and different concentrations of M35 constructs were rapidly mixed by vortexing, and absorbance at 340 nm was monitored as a function of time on a Jasco V-560 spectrophotometer.

Rubisco activity assay. Rubisco enzymatic activity was assayed at 25°C as described previously^{21,33}. Rubisco (0.25 µM) was incubated with M35 or variants (2 µM) for 15 min in buffer A unless indicated otherwise. Rubisco carboxylation activity was determined in buffer A containing RuBP (2 mM), NaHCO₃ (30 mM) and trace amount of radioactive NaH¹⁴CO₃ (0.33–0.5 mM; specific activity 40–60 mCi/mmol). After carbon fixation by Rubisco for 2 min, reactions were stopped with formic acid, and the amount of fixed carbon quantified using a

HITACHI AccuFLEX LSC-8000 scintillation counter. The activity of purified *SeRbcL₈S₈* is set to 100 %.

Liquid-liquid phase separation assay. For analysis of LLPS²⁵, reduced or oxidized M35 were labeled at the N-terminus with the fluorophore NT-650-NHS (NT650; NanoTemper) according to the manufacturer's instructions (~0.6 and ~0.4 dye molecules bound per M35 molecule, respectively). Rubisco holoenzyme was labeled at the N-terminus with the fluorophore Alexa FluorTM 532 NHS ester (ThermoFisher) according to the manufacturer's instructions (~2.6 dye molecules bound per Rubisco holoenzyme). NT650-M35 or A532-Rubisco was mixed with unlabeled M35 or unlabeled Rubisco at a ratio of 1:10 (1 μ M and 0.25 μ M total, respectively). 20 μ L reactions in buffer A with or without DTT with M35 (1 μ M) or Rubisco (0.25 μ M) alone or in combination were incubated for 10 min at 25°C before analysis by microscopy. For the M13-2 competition experiments, excess M13-2 (25 μ M) was added to the preformed Rubisco:M35 liquid droplets. The 20 μ L samples were transferred to an uncoated chambered coverslip (μ -Slide angiogenesis; ibidi) and illuminated with a coolLED pe-4000 LED source at 635 nm and 460 nm for fluorescence imaging and a 12 V/100 W halogen lamp for bright-field imaging. Images were recorded by focusing on the bottom of the plate using a Leica DMI6000B microscope with a Leica DFC900 GT sCMOS camera and a HCX PL APO 63x/1.20 water objective.

FRAP measurements. Fluorescence recovery after photobleaching (FRAP)³⁴ experiments for Rubisco condensates formed with M35 (containing 10 % NT650-M35, final 2 μ M) and unlabeled Rubisco (0.5 μ M) were carried out with a Leica TCS SP8 AOBS Confocal Laser

Scanning Microscope (HCX PL APO 63x/1.2 water objective, PMT detector). Images before and after photobleaching were recorded in a single focal plane at a 5 s time interval. Bleaching was performed using a 488 nm argon laser at 100 % intensity in 5 repeats with a dwell time 100 ms. The software Fiji was used for image analysis³⁵.

Dual-color fluorescence cross-correlation spectroscopy (dcFCCS). DcFCCS was performed as previously described³⁶. 0.25 μ M Rubisco (containing 2 nM N-terminal labeled Rubisco with Alexa FluorTM 532 NHS ester) and 1 μ M M35 (containing 2 nM N-terminal labeled M35 with NT-650-NHS) were mixed in buffer A and incubated for 5 min. To follow the displacement of M35 from Rubisco, preformed Rubisco:M35 complexes as above were incubated with an excess amount of M13-2 (25 μ M) for 5 min. The measurements were performed on a MicroTime 200 inverse time-resolved, confocal fluorescence microscope (PicoQuant) for 30 min. The auto-correlation data were fitted with one triplet one-diffusion equation using the Symphotime software (PicoQuant)³⁶.

Generation of ccmM mutants for analysis *in vivo*. Genetic sequences containing codon modifications, giving rise to serine residues instead of cysteine at positions C261, C279, C377 and C395 of the *Se7942 ccmM* gene, were synthesized (Genscript, U.S.A.) and inserted in pUC57-Amp^R. Each 989 bp synthetic sequence was supplied with 5' NcoI and 3' NotI restriction sites bordering the SSUL1 and SSUL2 domain regions of the native *ccmM* gene. These fragments were cloned into the pSE41 expression vector harboring the native *ccmM* gene sequence and transformed into a $\Delta ccmM$ mutant line^{10,37} (Extended Data Table 2).

Phenotypic analysis. Each *Se7942* strain was first grown over 2–3 days at ~3.0 % (v/v) CO₂ and then diluted in fresh modified BG11 medium to an optical density (OD₇₃₀) of 0.1 in triplicate 35 mL cultures. Cultures were grown at 30°C, 80 μmol of photons·m⁻²·s⁻¹ and bubbled with air or 3 % CO₂. Hourly culture measurements (OD_{730nm}) were conducted over a period of 8 h and the maximum growth rate was determined from the slope of logarithmic regressions of the data and transformed into doubling times¹⁰.

Wild-type and mutant *Se7942* strains were assessed for differences in photosynthetic affinity for inorganic carbon (C_i) by estimation of O₂ evolution rates over a range of C_i concentrations (0.01–250 mM) using an Oxylab O₂ electrode (Hansatech Instruments). Cultures were pre-grown at 3 % CO₂ and cells collected by centrifugation (5,000 × g, 5 min) and washed twice in an N₂-sparged version of BG-11 medium³⁸, buffered with 50 mM BisTrisPropane-HCl pH 7.9, containing 20 mM NaCl instead of NaNO₃. Washed cells were assayed at a chlorophyll density of 2 μg mL⁻¹ at 30°C, and light maintained at 170 μmol photons·m⁻²·s⁻¹ in an initial volume of 1.5 mL. Increasing C_i was supplied as NaHCO₃ from concentrated stock solutions prepared in water.

***In vivo* CcmM and Rubisco analysis.** The presence of CcmM and Rubisco proteins in *Se7942* strains was determined by immunoblot, essentially as described in ref. 39 with the following modifications: Cells pre-grown at 3 % CO₂ were harvested by centrifugation and resuspended in TE buffer (10 mM Tris-HCl pH 8.0, 1 mM EDTA) containing 1 % bacterial protease inhibitor cocktail, 700 mM mannitol and r-lysozyme (Merck) and Cell Lytic B (Sigma-Aldrich) and left shaking for 60 min at 37°C in darkness before being harvested by centrifugation and resuspended in a mannitol free TE buffer. Cells were lysed using an Emulsiflex (Avestin) set at

60 psi. Cell debris was removed by centrifugation ($3,000 \times g$, 10 min) and the clarified lysates were treated with 25 mM MgSO_4 to generate carboxysome-enriched pellet fractions as described previously^{40,41}. Clarified lysate samples containing approximately 100 ng chlorophyll and equivalent volumes of resuspended Mg^{2+} pellets and Mg^{2+} supernatants were diluted in SDS-PAGE sample buffer and proteins were separated on 4–20 % SDS-PAGE gels (Bio-Rad) prior to transfer to polyvinylidene fluoride (PVDF) membranes using a Trans-Blot Turbo blotting apparatus (Bio-Rad). Membranes were probed with polyclonal rabbit antiserum raised against Se7942 M35, and a polyclonal rabbit antiserum raised against *Nicotiana tabacum* Rubisco¹⁰. Bound antibodies were detected using alkaline phosphatase conjugated secondary antibodies and the Attophos AP fluorescent substrate system (Promega) and visualized by fluorescent detection using a ChemiDoc MP gel imaging system (BioRad).

Clarified cell lysates, carboxysome-enriched Mg^{2+} pellets and their corresponding supernatants were also used for Rubisco assays. These were carried out in 250 μL reaction volumes in assay buffer (100 mM EPPS pH 8.0, 20 mM MgCl_2 , 20 mM $\text{NaH}^{14}\text{CO}_3$; specific activity of $\text{NaH}^{14}\text{CO}_3$ is $\sim 800 \text{ cpm nmol}^{-1}$) at 25°C . Rubisco-containing samples (5 μL) were activated in the reaction mixture for 5 min prior to initiation of reactions by addition of 5 μL 20 mM RuBP. Reactions were allowed to proceed for 5 min and terminated by the addition of 250 μL 10 % (v/v) formic acid. Samples were dried overnight at 60°C before resuspension in 100 μL water and 1 mL Ultima Gold scintillation cocktail (PerkinElmer) and counted using a Tricarb 2800TR scintillation counter (PerkinElmer).

Size-exclusion chromatography coupled to multi-angle static light scattering (SEC-MALS).

M13-1 ($\sim 80 \mu\text{g}$) was analyzed using static and dynamic light scattering by auto-injection of the

sample onto a SEC column (5 μ m, 4.3x300 mm column, Wyatt Technology, product # WTC-030N5) at a flow rate of 0.15 mL min⁻¹ in buffer (20 mM MOPS-KOH pH 7.5, 100 mM KCl, 5 mM Mg(OAc)₂) at 25°C. The column is in line with the following detectors : a variable UV absorbance detector set at 280 nm (Agilent 1100 series), the DAWN EOS MALS detector (Wyatt Technology, 690 nm laser) and the Optilab rEXTM refractive index detector (Wyatt Technology, 690 nm laser)⁴². Masses were calculated using the ASTRA software (Wyatt Technology) with the dn/dc value set to 0.185 mL g⁻¹. Bovine serum albumin (Thermo) was used as the calibration standard.

Crystallization. The CcmM SSUL1 construct used for crystallization comprises residues 225–313 of CcmM from *Synechococcus elongatus* PCC7942. Because of a cloning artifact, the construct contains an N-terminal 3 amino acid extension of the sequence Ser/Glu/Phe.

CcmM SSUL1 oxidized: Crystals were grown by the sitting-drop vapor diffusion method at 4°C. Drops containing 500 nL of 25 mg mL⁻¹ CcmM SSUL1 in 10 mM Tris-HCl pH 6.8, 10 mM NaCl and precipitant were equilibrated against a large volume of precipitant. The precipitant contained 25.5 % PEG-3350 and 0.1 M Na-acetate pH 4.5.

CcmM SSUL1 reduced: Crystals were grown by the sitting-drop vapor diffusion method at 4°C. Drops containing 500 nL of 25 mg mL⁻¹ CcmM SSUL1 in 10 mM Tris-HCl pH 6.8, 10 mM NaCl, 10 mM DTT and precipitant were equilibrated against a large volume of precipitant. The precipitant contained 1.95 M ammonium sulfate and 0.1 M Na-acetate pH 4.5.

The crystals were transferred into cryo solution (precipitant/10 % (v/v) glycerol) and subsequently vitrified in liquid nitrogen.

Crystallographic data collection and structure solution. The diffraction data of the crystals of CcmM SSUL1 in the disulfide-bonded state were collected at beamline ID23-2 at the European Synchrotron Radiation Facility (ESRF) in Grenoble, France.

The diffraction data of the crystals of CcmM SSUL1 in the thiol-reduced state were collected at the automated beamline ID30A-1 at the European Synchrotron Radiation Facility (ESRF) in Grenoble, France.

Diffraction data were integrated with XDS and further processed with POINTLESS⁴³, AIMLESS⁴⁴ and CTRUNCATE⁴⁵ as implemented in the CCP4i graphical user interface⁴⁶. The structure of disulfide-bonded CcmM SSUL1 was solved by molecular replacement at 1.65 Å resolution using the program MOLREP⁴⁷ using the SSUL domain of *Nostoc sp.* PCC7120 Rubisco activase-like protein (PDB 6HAS, unpublished structure) as a search template. The asymmetric unit contained two copies of the SSUL1 domain. The model was edited manually using Coot⁴⁸. REFMAC5⁴⁹ was used for model refinement. The model of SSUL1_{ox} contains 97 ordered water molecules and exhibits reasonable stereochemistry with 98.8 % of the residues in the favored regions of the Ramachandran plot according to the criteria of MolProbity⁵⁰. The structure of SSUL1 in the thiol-reduced state was solved at 1.2 Å resolution by molecular replacement using the disulfide-bonded model and refined as described above. The asymmetric unit contained two copies of the SSUL1 domain, seven sulfate ions and 162 ordered water molecules. According to MolProbity⁵⁰, the model of SSUL1_{red} exhibits excellent stereochemistry with 98.9 % of the residues in the favored regions of the Ramachandran plot. Figures were created with PyMol (<http://www.pymol.org/>) and ESPript⁵¹.

The crystallographic models and structure factors have been deposited to www.PDB.org under accession codes 6HBA (oxidized) and 6HBB (reduced), respectively.

Transmission electron microscopy. *Se7942* cells were grown in modified BG-11 medium³⁸ containing 20 mM HEPES-KOH pH 8.0, at 3 % CO₂, 30 °C and approximately 80 μmol photons m⁻² s⁻¹ over 2–3 days. Cells in 10 mL of culture were fixed for at least 4 h with an equal volume of 8 % formaldehyde/5 % glutaraldehyde (ProSciTech) and 200 mM piperazine-N,N'-bis(2-ethanesulfonic acid) pH 7.2 (PIPES; Sigma-Aldrich). Cells were centrifuged at 5,000 × g for 5 min, washed 3 times with 100 mM PIPES, and then fixed in 1 % (w/v) osmium tetroxide for 4 h. Fixed cells were dehydrated through an ethanol series and embedded in LR white resin (ProSciTech). Ultrathin sections were obtained and stained with 2 % (w/v) uranyl acetate and lead citrate and viewed using a Hitachi H7100FA TEM.

Cryo-electron microscopy for single particle analysis. Rubisco (6.25 μM) and M35 (50 μM) were mixed in buffer A and incubated at 25°C for 10 min, then 10 nm Au₁₃-BSA tracer (AURION) was added. Holey carbon supported copper-grids (Quantifoil R2/1 300 mesh) were plasma-cleaned for 30 s (Harrick Plasma) before using. All cryo-grids were made using a Vitrobot Mark 4 (FEI), 3 μL solution were added to a grid at 25°C and 90 % humidity, then semi-automatically blotted and plunge-frozen into liquid ethane.

Grids were first screened on a Talos Arctica (FEI) transmission electron microscope (TEM). Selected grids were transferred to a Titan Krios 300 kV TEM (FEI) equipped with GIF Quantum Energy Filters (Gatan), and imaged with a K2 Quantum direct detector (Gatan) operated in movie mode at 0.15 s per frame, with 0.822 Å pixel size and 7 s exposure. 4,723 movies were collected automatically by SerialEM⁵².

MotionCor2⁵³ was first applied to the movies with dose-weighting. 7,520 particles were picked manually and templates for auto-picking were generated from the 2D classification using RELION 2.1⁵⁴. The selected 2D classes were used in Gautomatch (<http://www.mrc-lmb.cam.ac.uk/kzhang/Gautomatch>), yielding 988,648 particles in total (Extended Data Fig. 6d). RELION 2.1 was used for further data processing. The complete data set went through one round of 2D classification to remove bad particles, such as ice and particles on carbon, followed by 3D classification of 663,599 particles (Extended Data Fig. 6d). An initial model was generated using RELION and further refined using 83,746 cleaned particles. No symmetry was applied in these procedures. 3D classification of 663,599 particles resulted in 4 classes, with only one (class 3) showing preferred orientation (Extended Data Fig. 6d). Class 1 comprising 29 % of particles was first selected and refined. The refined map showed extra density (equivalent to two SSUL modules associated with Rubisco) between anti-parallel RbcL dimers (Extended Data Fig. 6d, scheme on the left). To determine how many SSUL domains bind per site, the extra density was extracted and a focused classification carried out with a reference and a mask covering two SSUL modules. This showed that in 3 major classes only one SSUL domain was bound per site, either above or below the equator of the Rubisco holoenzyme (Extended Data Fig. 6d, scheme on the left). Next, we extracted units containing 2 RbcL, 2 RbcS and 2 SSUL for classification and refinement (Extended Data Fig. 6d, main scheme). Before subtraction, particles were first aligned using D4 symmetry and then the symmetry was expanded using the `relion_particle_symmetry_expand` command to generate eight-fold aligned particles. The two best resolved classes (class v and vi) contain 78,916 and 103,669 particles, respectively, and were used for final particle refinement with local alignment, resulting in 2.77 and 2.84 Å maps, respectively, after post-processing (Extended Data Fig. 6d). Only class v with the best resolution

was then used for model building. Local resolution was calculated using ResMap⁵⁵ and RELION. The crystal structures of thiol-reduced SSUL1 and RbcL and RbcS (PDB 1RBL) were placed into the density using Chimera (v 1.12). The model was edited with Coot⁴⁸. The model was refined in reciprocal space against a masked map with REFMAC5⁴⁹. Residues with disordered side-chains were modeled as alanine. The program CONTACT (Tadeusz Skarzynski, Imperial College, London) as implemented in the CCP4i graphical user interface was employed to analyze the intermolecular interactions using 4 Å as cut-off distance.

The model and the electron density has been deposited to www.PDB.org and the EM database under accession codes 6HBC and EMD-0180, respectively.

Cryo-electron tomography. For analysis of the Rubisco:M35 network, Rubisco (6.25 µM) was mixed with M35 (50 µM) in buffer A. For analysis of the Rubisco:M24-1/2 network, Rubisco (6.25 µM) was mixed with M24-1/2 (50 µM) in buffer A. The mixtures were incubated for 10 min at 25°C. The Rubisco:M24-1/2 reaction was diluted 2-fold before cryo-grid preparation. Cryo-grids were prepared as described above for single particle analysis.

Rubisco:M35 grids were pre-screened on a Talos Arctica (FEI) TEM and suitable grids then transferred to a Titan Krios 300 kV TEM (FEI) equipped with a GIF Quantum Energy Filters (Gatan), and imaged with a K2 Summit direct detector (Gatan) operated in movie mode at 5 frames per second. Using SerialEM⁵², dose symmetric tilt-series were recorded from –60° to +60° (in two halves separated at 0) in 2° increments, with a pixel size of 2.234 Å, a target defocus of –4.5 µm, and a cumulative electron dose of 60 electrons/Å². For the Rubisco:M24-1/2 complex, single-axis tilt-series were recorded automatically using SerialEM, from –60° to +60° (in two halves separated at 0) in 2° increments on Talos Arctica TEM (FEI), equipped with a

Falcon 3EC Direct Electron Detector (FEI) with a pixel size of 1.977 Å. Image frames were first aligned using MotionCor2, then etomo (IMOD version 4.10.15)⁵⁶ was used for alignment and generation of a 4-times binned tomogram. Template matching was performed using PyTom⁵⁷. The template was generated from the single particle reconstruction map and low-pass filtered to 40 Å resolution. Spherical masks were used in template matching. For each tomogram, the highest cross-correlation peaks were exhaustively extracted with a spherical mask of radius of 64 Å. Particles were manually selected, amounting to 2685 particles for Rubisco:M35 and 1813 for Rubisco:M24-1/2. Nearest neighbor distances were determined according to the coordinates from template matching with the TOM Toolbox in Matlab and simulated tomogram volumes were generated, according to the coordinates and orientations from template matching. Only particles in the condensate whose distance from nearest neighbor fits the plausible range (100 Å to 420 Å for Rubisco:M35 and 100 Å to 280 Å for Rubisco:M24-1/2) were selected for statistical analysis. Analysis according to Mann-Whitney test showed no significant difference between the measured distances for Rubisco:M35 and Rubisco:M24-1/2 ($p < 0.05$).

Reporting summary. Further information on experimental design is available in the Nature Research Reporting Summary linked to this paper.

Data availability. The crystallographic models and structure factors for SSUL1_{ox} and SSUL1_{red} have been deposited to wwPDB under accession codes 6HBA (oxidized) and 6HBB (reduced), respectively. The electron density reconstructions and final 2RbcL:2RbcS:SSUL model have been deposited in the Electron Microscopy Data Bank (EMDB) and wwPDB under accession codes EMD-0180 and 6HBC, respectively. Source data for graphs can be found in Graphical

Source Data Fig. 1-3 and the source data for the gels shown in Extended Data Fig. 5b in
Supplementary Fig. 1.

- 29 Catanzariti, A. M., Soboleva, T. A., Jans, D. A., Board, P. G. & Baker, R. T. An efficient system for high-level expression and easy purification of authentic recombinant proteins. *Protein Sci.* **13**, 1331-1339 (2004).
- 30 Liu, C. *et al.* Coupled chaperone action in folding and assembly of hexadecameric Rubisco. *Nature* **463**, 197-202 (2010).
- 31 Saschenbrecker, S. *et al.* Structure and function of RbcX, an assembly chaperone for hexadecameric Rubisco. *Cell* **129**, 1189-1200 (2007).
- 32 Riddles, P. W., Blakeley, R. L. & Zerner, B. Reassessment of Ellman's reagent. *Methods Enzymol.* **91**, 49-60 (1983).
- 33 Brinker, A. *et al.* Dual function of protein confinement in chaperonin-assisted protein folding. *Cell* **107**, 223-233 (2001).
- 34 Maharana, S. *et al.* RNA buffers the phase separation behavior of prion-like RNA binding proteins. *Science* **360**, 918-921 (2018).
- 35 Schindelin, J. *et al.* Fiji: an open-source platform for biological-image analysis. *Nat. Methods* **9**, 676-682, (2012).
- 36 Gupta, A. J., Haldar, S., Milicic, G., Hartl, F. U. & Hayer-Hartl, M. Active cage mechanism of chaperonin-assisted protein folding demonstrated at single-molecule level. *J. Mol. Biol.* **426**, 2739-2754 (2014).
- 37 Woodger, F. J., Badger, M. R. & Price, G. D. Sensing of inorganic carbon limitation in *Synechococcus* PCC7942 is correlated with the size of the internal inorganic carbon pool and involves oxygen. *Plant Physiol.* **139**, 1959-1969 (2005).
- 38 Price, G. D. & Badger, M. R. Ethoxymethylamine inhibition of CO₂-dependent photosynthesis in the cyanobacterium *Synechococcus* PCC7942. *Plant Physiol.* **89**, 44-50 (1989).
- 39 Long, B. M., Tucker, L., Badger, M. R. & Price, G. D. Functional cyanobacterial beta-carboxysomes have an absolute requirement for both long and short forms of the CcmM protein. *Plant Physiol.* **153**, 285-293 (2010).
- 40 Price, G. D. & Badger, M. R. Evidence for the role of carboxysomes in the cyanobacterial CO₂-concentrating mechanism. *Can. J. Bot.* **69**, 963-973 (1991).
- 41 Price, G. D., Sültemeyer, D., Klughammer, B., Ludwig, M. & Badger, M. R. The functioning of the CO₂ concentrating mechanism in several cyanobacterial strains: a review of general physiological characteristics, genes, proteins, and recent advances. *Can. J. Bot.* **76**, 973-1002 (1998).
- 42 Wyatt, P. J. Light scattering and the absolute characterization of macromolecules. *Anal. Chim. Acta* **272**, 1-40 (1993).
- 43 Evans, P. Scaling and assessment of data quality. *Acta Crystallogr. D Biol. Crystallogr.* **62**, 72-82 (2006).
- 44 Evans, P. R. & Murshudov, G. N. How good are my data and what is the resolution? *Acta Crystallogr. D Biol. Crystallogr.* **69**, 1204-1214 (2013).
- 45 French, G. & Wilson, K. On the treatment of negative intensity observations. *Acta Crystallogr. Sect. A* **34**, 517-525 (1978).
- 46 Potterton, E., Briggs, P., Turkenburg, M. & Dodson, E. A graphical user interface to the CCP4 program suite. *Acta Crystallogr. D Biol. Crystallogr.* **59**, 1131-1137 (2003).
- 47 Vagin, A. & Teplyakov, A. Molecular replacement with MOLREP. *Acta Crystallogr. D Biol. Crystallogr.* **66**, 22-25 (2010).

- 48 Emsley, P. & Cowtan, K. Coot: model-building tools for molecular graphics. *Acta Crystallogr. D Biol. Crystallogr.* **60**, 2126-2132 (2004).
- 49 Murshudov, G. N. *et al.* REFMAC5 for the refinement of macromolecular crystal structures. *Acta Crystallogr. D Biol. Crystallogr.* **67**, 355-367 (2011).
- 50 Chen, V. B. *et al.* MolProbity: all-atom structure validation for macromolecular crystallography. *Acta Crystallogr. D Biol. Crystallogr.* **66**, 12-21 (2010).
- 51 Gouet, P., Courcelle, E., Stuart, D. I. & Metoz, F. ESPript: multiple sequence alignments in PostScript. *Bioinformatics* **15**, 305-308 (1999).
- 52 Mastronarde, D. N. Automated electron microscope tomography using robust prediction of specimen movements. *J. Struct. Biol.* **152**, 36-51 (2005).
- 53 Zheng, S. Q. *et al.* MotionCor2: anisotropic correction of beam-induced motion for improved cryo-electron microscopy. *Nat. Methods* **14**, 331-332 (2017).
- 54 Scheres, S. H. RELION: implementation of a Bayesian approach to cryo-EM structure determination. *J. Struct. Biol.* **180**, 519-530 (2012).
- 55 Kucukelbir, A., Sigworth, F. J. & Tagare, H. D. Quantifying the local resolution of cryo-EM density maps. *Nat. Methods* **11**, 63-65 (2014).
- 56 Kremer, J. R., Mastronarde, D. N. & McIntosh, J. R. Computer visualization of three-dimensional image data using IMOD. *J. Struct. Biol.* **116**, 71-76 (1996).
- 57 Hrabe, T. *et al.* PyTom: a python-based toolbox for localization of macromolecules in cryo-electron tomograms and subtomogram analysis. *J. Struct. Biol.* **178**, 177-188 (2012).

EXTENDED DATA FIGURE LEGENDS

Extended Data Fig. 1 | Crystal structure and sequence analysis of the SSUL domains. **a**, Ribbon representation of the asymmetric unit in the crystal lattice of the SSUL1 domain in the thiol-oxidized state. A view along the approximate dyad axis is shown. The two copies of SSUL1 with nearly identical conformations (with C α r.m.s.d. 0.43 Å) are shown in magenta and cyan, respectively. Secondary structure elements and chain termini are indicated. **b**, SEC-MALS analysis of purified SSUL1. The red dotted line across the peak indicates molar mass and homogeneity of the protein sample. The molar mass is indicated (calculated theoretical mass is 10537.7 Da). A representative experiment is shown ($n=2$ independent experiments). **c**, Sequence alignment of the SSUL domains 1–3 in CcmM and RbcS from *Synechococcus elongatus* sp. PCC7942. Amino acid sequences were aligned using the EBI Clustal- Ω server. Secondary structure elements for the SSUL1 domain are indicated above the sequences. Residues that are similar between SSUL (group 1) and RbcS (group 2) are boxed with blue frames; identical residues are shown in white on a red background. Triangles below the sequence indicate the contact residues of RbcS with the RbcL₈ core in the Rubisco complex. The mutation site in the SSUL1 module (R251/R252) is indicated. The stars in magenta above the sequence indicate the contact residues of SSUL in the complex with Rubisco. Note that these residues are generally highly conserved in other β -cyanobacteria. The cysteine residues conserved in SSUL1 and SSUL2 are in bold and with yellow background. Note that SSUL1 and SSUL2 share 84 % identity, while SSUL3 is more divergent (58 % identity with SSUL1). **d**, Surface properties of the SSUL1 domain. Hydrophobic side-chains are indicated in yellow. Red and blue represent negative and positive charges, respectively. Dashed boxes indicate two areas of charge clusters. **e**, Ribbon representation of the asymmetric unit in the crystal lattice of the SSUL1 domain in the thiol-reduced state. A view along the approximate dyad axis is shown. The two copies of SSUL1 are shown in gold and blue, respectively. Secondary structure elements and chain termini are indicated. **f**, Overlay of SSUL1 structures in the oxidized (magenta) and reduced (gold) forms.

Extended Data Fig. 2 | Properties of the Rubisco:M35 network. **a**, SDS-PAGE of recombinantly expressed and purified proteins. A representative SDS gel is shown ($n=3$ independent experiments). **b**, Rubisco carboxylation activity of the reactions shown in Fig 1e, including RbcL₈ core complexes and RbcS in the absence of M35. The activity of purified RbcL₈S₈ is set to 100 %, equivalent to a k_{cat} of $\sim 4 \text{ s}^{-1}$ per active site (dark grey bar). Data are mean \pm s.d. ($n=3$ independent experiments). **c**, Kinetics of M35-mediated network formation of Rubisco and Rubisco assembly intermediates by turbidity assay in buffer A at 25°C. RbcL₈ core complexes (0.25 μM) were incubated with RbcX from *Anabaena* sp. CA (8 μM), or the cognate Raf1 (2 μM) or BSD2 from *Arabidopsis thaliana* (4 μM) in buffer A for 15 min to generate the respective Rubisco assembly intermediates. M35 (2 μM) was then added to start the turbidity measurement at 340 nm. Turbidity of Rubisco with M35 is shown as control. A representative experiment is shown ($n=3$ independent experiments). **d**, Kinetics of network formation of Rubisco (0.25 μM) with M35 (2 μM) or with combined M13-1, M13-2 and M13-3 (2 μM each) by turbidity assay in buffer A at 25°C. A representative experiment is shown ($n=3$ independent experiments). **e**, Kinetics of network formation by turbidity assay at 25°C of unlabeled Rubisco (0.25 μM) with M35 N-terminally labeled with the fluorophore NT-650-NHS (NT650-M35; 1

μM) and of unlabeled M35 (1 μM) with Rubisco N-terminally labeled with Alexa Fluor™ 532 NHS ester (A532-Rubisco; 0.25 μM). A reaction containing unlabeled Rubisco (0.25 μM) and unlabeled M35 (1 μM) is shown as control. A representative experiment is shown ($n=3$ independent experiments). **f**, dcFCCS of 0.25 μM Rubisco (containing 2 nM A532-Rubisco) and 1 μM M35 (containing 2 nM NT650-M35). Measurements were taken for 30 min after 5 min incubation in buffer A. Cross-correlation curves are shown. After formation of the Rubisco:M35 network, unlabeled M13-2 (25 μM) was added and cross-correlation measured for 30 min. Auto-correlation curves of 0.25 μM Rubisco (containing 2 nM A532-Rubisco) and 1 μM M35 (containing 2 nM NT650-M35) are also shown. The diffusion coefficients (D) are indicated. The relatively slow rate of diffusion of M35 suggests that the protein is expanded and not as compact as would be expected for a protein of ~ 35 kDa. To exclude the possibility that the slow diffusion rate of M35 is due to interactions between M35 molecules, we also measured the auto-correlation of M35 at very low concentration (2 nM NT650-M35), where protein-protein interactions are unlikely, and found the same rate of diffusion. Data are the mean \pm s.d. ($n=3$ independent experiments).

Extended Data Fig. 3 | Salt sensitivity of M35-Rubisco interaction. **a**, Kinetics of Rubisco network formation by turbidity assay at different salt concentrations at 25°C. Rubisco (0.25 μM) in the presence of 2 μM M35_{red} in buffer (50 mM Tris-HCl pH 8.0, 10 mM Mg(OAc)₂, 5 mM DTT) containing different concentrations of KCl at 25°C. A representative experiment is shown ($n=3$ independent experiments). **b**, Kinetics of Rubisco network formation as in (a) at 50 mM and 150 mM KCl, and higher concentrations of Rubisco (0.5 or 1.0 μM) and M35 (4.0 or 8.0 μM). A representative experiment is shown ($n=3$ independent experiments). **c**, Kinetics of Rubisco network formation by turbidity assay at different salt concentrations at 25°C as in (a) but in the presence of 2 μM M35_{ox} and in buffer without DTT. A representative experiment is shown ($n=3$ independent experiments). **d**, M35 function is redox-sensitive. Network formation of Rubisco (0.25 μM) by M35_{ox} (2 μM) was monitored in buffer (50 mM Tris-HCl pH 8.0, 10 mM Mg(OAc)₂) containing 100 mM KCl for 5 min, followed by addition of 5 mM DTT for further 10 min. Rubisco (0.25 μM) with M35_{red} (2 μM) in buffer containing 100 mM KCl/5 mM DTT is shown as control. A representative experiment is shown ($n=3$ independent experiments). **e-f**, Kinetics of Rubisco network formation by turbidity assay at different salt concentrations at 25°C as in (a) in the presence of 2 μM reduced M24-1/2 (e) and M24-2/3 (f). A representative experiment is shown ($n=3$ independent experiments).

Extended Data Fig. 4 | LLPS of Rubisco by M35_{red} and M35_{ox}. **a**, Size distribution of liquid droplets ($n=275$) formed by unlabeled Rubisco (0.25 μM) and M35 (1 μM , containing 10 % NT650-M35). The Feret's diameter for the main peak (indicated by arrow) and average size is 1.33 μm and 1.32 μm , respectively. **b**, Time lapse images of droplet fusion. Reactions containing labeled M35_{red} (1 μM , containing 10 % NT650-M35) and unlabeled Rubisco (0.25 μM) were observed over time. Droplets undergoing fusion are indicated by white arrow heads. Scale bar 10 μm . A representative experiment is shown ($n=3$ independent experiments). **c**, LLPS of Rubisco:M35_{ox} (left) and Rubisco:M35_{red} (right). NT650-M35_{ox} or NT650-M35_{red} was mixed with unlabeled M35_{ox} or M35_{red}, respectively, at a ratio of 1:10 (1 μM total) and imaged by

fluorescence microscopy at 25°C in combination with unlabeled Rubisco (0.25 μ M). Scale bar 10 μ m. A representative experiment is shown ($n=3$ independent experiments). **d**, Rubisco:M35_{red} condensates were generated as in (c) and imaged by fluorescence and bright-field microscopy at 25°C (panels 1 and 2). Dissociation of droplets was observed upon addition of unlabeled M13-2 (25 μ M) (panels 3 and 4) to preformed droplets as in panels 1 and 2. Scale bar 10 μ m. A representative experiment is shown ($n=3$ independent experiments).

Extended Data Fig. 5 | Role of disulfide bonds in SSUL in carboxysome function. a, Photosynthetic O₂ evolution in response to external Ci by *Se7942* WT and *ccmM* mutant strains. Shown is a representative set of Clarke-type oxygen electrode measurements of Ci-dependent O₂ evolution by different strains of *Se7942* from 10 μ M to 250 mM Ci. Cysteine mutants (C279S, C395S and CcmM-4S) were observed to have an intermediary CO₂ requiring phenotype, with CcmM-4S having the highest CO₂ requirement. A representative experiment is shown ($n=3$ biological replicates). **b**, Relative RbcL abundance in carboxysome-enriched pellet fractions in WT and CcmM mutant strains of *Se7942*. RbcL and CcmM proteins were detected using anti-RbcL and anti-M35 antibodies, respectively. A representative experiment is shown ($n=3$ biological replicates). **c**, Length:width ratios of carboxysomes in WT and CcmM mutant strains. Carboxysomes were visualized using TEM, and their length and width measured. These measurements were used to calculate the length:width ratio. Large increases in carboxysome length:width ratio were observed in cysteine mutants, particularly C279S and CcmM-4S. The numbers of carboxysomes analyzed in the different strains are indicated. The horizontal line represents the mean of each dataset. Whiskers indicate upper and lower data points of the range. The number of measured values (n) is indicated above each dataset. **d**, Cell cross-sections for WT and *ccmM* mutant strains analyzed by TEM and carboxysomes per cell section counted. Cell sections (WT $n=25$; $\Delta ccmM+ccmM$ $n=23$; C279S $n=28$; C395S $n=26$; CcmM-4S $n=25$) were analyzed and the data expressed as percent of the number of carboxysomes in WT \pm s.e.m. *, $p<0.05$; ***, $p<0.001$ (Tukey's multiple comparisons test). p -Values indicated for WT and $\Delta ccmM+ccmM$ versus cysteine mutants (WT versus CcmM-4S $p=0.0006$, WT versus C395S $p=0.0008$, $\Delta ccmM+ccmM$ versus CcmM-4S $p=0.0397$, $\Delta ccmM+ccmM$ versus C395S $p=0.0464$).

Extended Data Fig. 6 | Cryo-EM single particle reconstruction. a, A representative micrograph of Rubisco:M35 complexes used for single particle reconstruction ($n=4,723$ micrographs from one EM grid). **b**, The 2D class averages of complexes in (a) showing extra-density of SSUL-bound to Rubisco in some classes. **c**, Meshwork representation of unsharpened D4 symmetry-averaged electron density map of the Rubisco:M35 complex (at a contour level of 2.8σ , appropriate for Rubisco), with the D4-averaged final model in backbone trace representation superposed (top). Shown below is the zoomed-in region. Note that there is only ~50 % residual density for the two SSUL modules, except for the region where the modules overlap in the center (helices $\alpha 1$). **d**, The workflow for single particle data processing. The left scheme of the flowchart identified only one SSUL domain bound between 2 RbcL subunits. The main scheme took the units consisting of 2 RbcL, 2 RbcS and 2 SSUL for focused classification and further refinement to improve the map quality. See Methods for details. **e**, Gold-standard FSC corrected curve (masked and B-factor sharpened) of the final 3D reconstruction. The resolution is ~2.77 Å at the FSC cutoff of 0.143.

Extended Data Fig. 7 | Cryo-EM single particle reconstruction. **a**, Local resolution for the refined map of class v (2RbcL:2RbcS:SSUL) particles (see Extended Data 6d). The color gradient from blue to red indicates local resolution from 2.0 to 4.0 Å. Right panel shows zoomed-in views of the solvent facing side and the buried interaction side of SSUL. As expected, the elements facing Rubisco have higher resolution. **b**, Quality of the cryo-EM density map of SSUL and the structural model of 2RbcL:2RbcS:SSUL in the vicinity of some aromatic side-chains of SSUL1. The density is shown as a meshwork in cyan. The backbone of the structural model is in ribbon representation, and side-chains are shown in stick representation. The cryo-EM map is shown at 1.2σ . **c-d**, Cryo-EM density map for SSUL at interface I (c) and interface II (d), respectively. Structural features of interface I. Critical interacting residues (see Fig. 4c): Phe253^{SSUL} forms van-der-Waals contacts to His353^{RbcL-A}/Glu355^{RbcL-A} and Arg254^{SSUL} forms interactions with Glu351^{RbcL-A} and a backbone-backbone H-bond with His353^{RbcL-A}. The side-chain of Arg251^{SSUL} is sandwiched between RbcS residues Gln36/Gly37 and Asn94/Ile95, and forms a salt-bridge with Asp93^{RbcS}. Arg252^{SSUL} forms a salt-bridge with Asp76^{RbcL-B}. Thr255^{SSUL} and Ser257^{SSUL} form additional contacts with Arg79^{RbcL-B} and Asp76^{RbcL-B}. Structural features of interface II. Critical interacting residues (see Fig. 4d): Ile293^{SSUL} contacts Thr30^{RbcL-B}, Arg298^{SSUL} makes van-der-Waals interactions with Tyr85^{RbcL-B} and His86^{RbcL-B}, and Arg300^{SSUL} with Tyr29/Thr30/Pro31/Lys32 in RbcL-B. **e**, Circular dichroism wavelength scans. CD wavelength scans of M35-WT and the mutant M35-R251D/R252D (3.5 μM each) in buffer (50 mM KH₂PO₄ pH 7.5) measured at 25°C with 0.1 cm cuvettes using a Jasco 715 CD spectrometer. **f**, Dependence of Rubisco:M35 interaction on interface I contacts and RbcS. RbcL₈ (0.25 μM) and RbcS (2.5 μM) were mixed in buffer A and incubated for 10 min, followed by addition of M35 or M35-R251D/R252D (1 μM each), and complex formation monitored by turbidity (black and green, respectively). The requirement of RbcS was analyzed by addition of RbcS to premixed RbcL₈ and M35. Arrow indicates time of RbcS addition. A representative experiment is shown ($n=3$ independent experiments). **g**, Inability of M35 mutant R251D/R252D to induce phase separation of Rubisco. Unlabeled M35-R251D/R252D (1 μM) was mixed with Rubisco (0.25 μM, containing 10 % A532-Rubisco) and imaged by bright field (left) and fluorescence microscopy (right) at 25°C (top panels). As control, unlabeled M35 (1 μM) was mixed with Rubisco (0.25 μM, containing 10 % A532-Rubisco) (bottom panels). Scale bar 10 μm. A representative experiment is shown ($n=3$ independent experiments).

Extended Data Fig. 8 | Cryo-ET of Rubisco:35 and Rubisco:M24-1/2 condensates. **a**, Analysis of the Rubisco:M35 condensate by cryo-ET. A slice through a tomographic volume of the matrix (left) and Rubisco:SSUL particles, from single particle reconstruction with C1 symmetry and low-pass filtered to 40 Å, rendered into a 3D matrix (right). The circled cluster of complexes is shown again in Fig. 4e. A representative tomogram is shown ($n=3$ independent tomograms of the same biological sample). **b**, Distribution of nearest neighbor center to center distances between Rubisco particles in tomograms of Rubisco:M35 (2654 particles analyzed) and Rubisco:M24-1/2 (1405 particles analyzed). Data are from $n=3$ tomograms for each sample. The schematic above the histogram shows the distance between two Rubisco particles relative to the maximum distance spanned by the linkers between SSUL modules in M35. **c**, Analysis of the Rubisco:M24-1/2 condensate by cryo-ET. A slice through a tomographic volume of the matrix

(left) and Rubisco:SSUL particles, from single particle reconstruction with C1 symmetry and low-pass filtered to 40 Å, rendered into a 3D matrix (right). A representative tomogram is shown ($n=3$ independent tomograms of the same biological sample).

Fig. 1

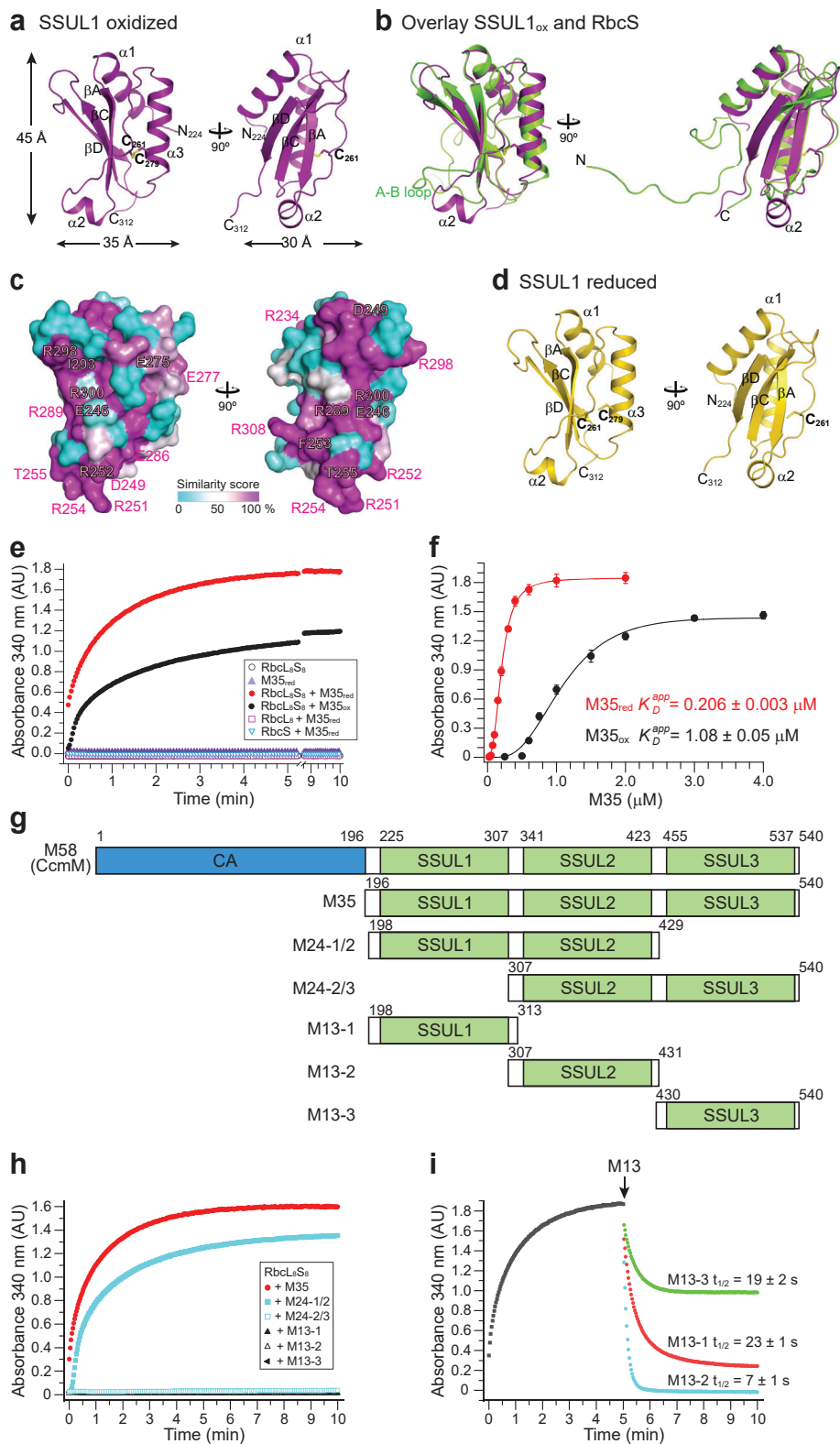


Fig. 2

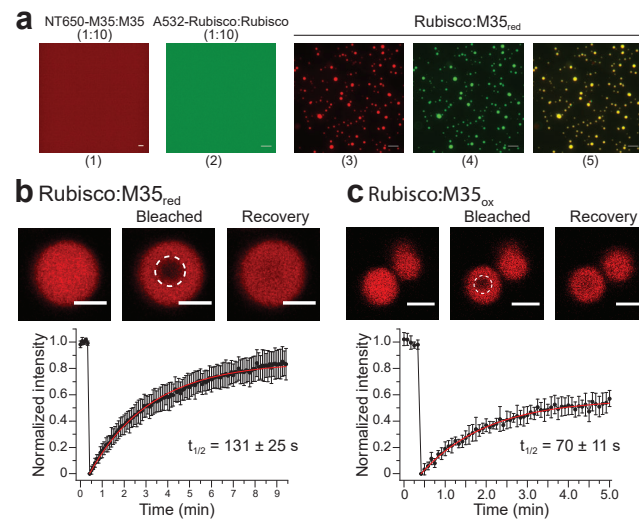


Fig. 3

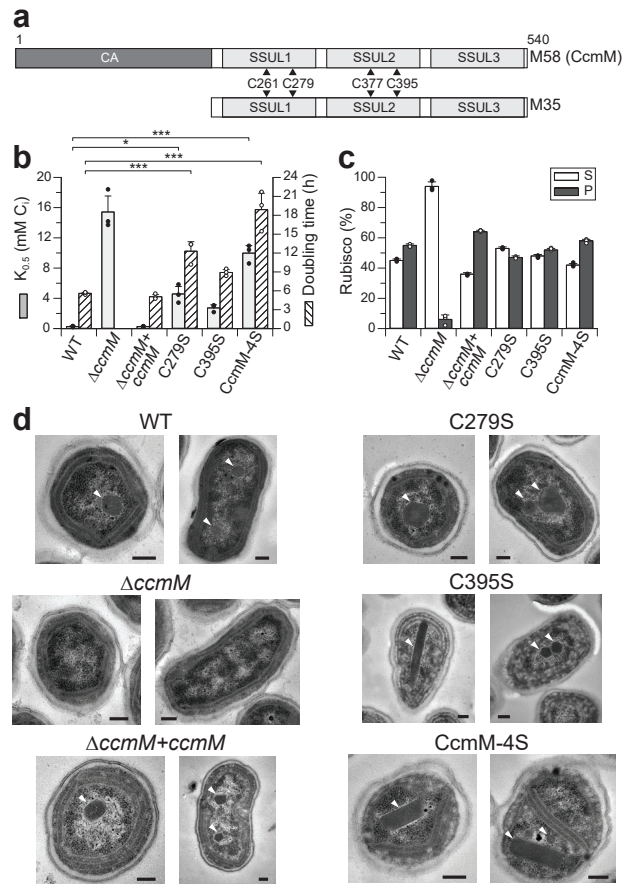


Fig. 4

